Materials Characterization 208 (2024) 113675

Contents lists available at ScienceDirect

Materials Characterization

journal homepage: www.elsevier.com/locate/matchar

Exploration and optimization of copper-based alloys incorporating amorphizing elements for heat transfer applications

I. Izaguirre [a,*], J. de Prado [a], J.J. Rosero-Romo [c], M. Sánchez [a,b], D. Salazar [c], A. Ureña [a,b]

[a] Materials Science and Engineering Area, ESCET, Rey Juan Carlos University, C/Tulipán s/n, 28933, Móstoles, Madrid, Spain
[b] Instituto de Tecnologías Para la Sostenibilidad, Universidad Rey Juan Carlos, C/ Tulipán s/n, 28933, Móstoles, Madrid, Spain
[c] BCMaterials, Basque Center for Materials, Applications, and Nanostructures, UPV/EHU Science Park, 48940 Leioa, Spain

ARTICLE INFO

Keywords:
Brazing
Fusion reactor
Tungsten
Flexible filler
Melt-spun ribbons
Amorphous alloys

ABSTRACT

Attaining an amorphous crystalline structure imparts unique properties to certain metallic alloys that are impossible to achieve with conventional crystalline alloys. This current study investigates the amorphization potential of small additions of Zr, Ni, or V in Cu—Ti alloys produced using the melt-spinning technique. The alloys are characterized using X-ray diffraction (XRD), differential thermal analysis (DTA), differential scanning calorimetry (DSC), and transmission electron microscopy (TEM) techniques.

The need for filler materials with flexible and adaptable properties for joining the first wall and divertor components of future fusion reactors can be addressed by producing filler ribbons with amorphous structures. The results indicate that a combination of Zr (12 at. %) and Ni (8 at. %), when used as alloying elements with appropriate processing parameters such as a rectangular nozzle of 0.5 × 8.8 mm^2 and a linear wheel speed of 30 m/s, can produce an amorphous structure. Only isolated nanocrystalline phases were detected by TEM analysis. As a result, ribbons fabricated under these conditions were several times longer and wider than those made using the Cu—Ti master alloy. More importantly, they exhibit enough flexibility to conform to and cover a simulated pipe of the reactor.

Conversely, the addition of V led to the formation of brittle phases. Ribbons fabricated under the optimal conditions were tested as filler materials in W-CuCrZr joints at 960 °C and were microstructurally and mechanically characterized, demonstrating their suitability for the intended application.

1. Introduction

The divertor plays a critical role in a fusion reactor, as it is responsible for extracting heat and particles from the plasma, enabling the preservation of plasma fusion reactions, even while enduring high levels of particle and heat input. In the context of fusion energy, the development of the DEMO reactor must aim to achieve plasma reactions with higher power density and longer pulse durations. Consequently, the effects of erosion and material degradation, as well as their impact on the overall performance and efficiency of the reactor, will be magnified [1–3]. Recent divertor design includes the incorporation of several auxiliary systems integrated with the divertor into the lower level of the machine. [4]. The pipes inside the divertor of a fusion reactor serve multiple functions such as cooling, material collection removing impurities, or control of plasma parameters, depending on their location and design [5]. Cooling pipes serve the crucial purpose of dissipating heat from the divertor components exposed to extremely high temperatures; otherwise, these components would rapidly degrade or even melt. Typically, they are constructed from materials boasting high thermal conductivity and excellent corrosion resistance, such as copper alloys or stainless steel [6]. These pipes must be securely connected to tungsten monoblocks, which face the plasma and act as a protective shield for the inner components. Both the pipes and monoblocks need to be joined using a technique that meets a set of requirements, including effective heat transmission, the ability to withstand high temperatures, and the flexibility to be manipulated as needed.

These criteria are satisfied by amorphous alloys, which possess unique mechanical, thermal, and electrical properties in comparison to crystalline materials due to the absence of a long-range ordered crystal structure. Specifically, metallic glasses can exhibit remarkable flexibility and exceptional mechanical properties, rendering them highly appealing for a wide range of applications. The disordered atomic

* Corresponding author.
E-mail address: ignacio.izaguirre@urjc.es (I. Izaguirre).

https://doi.org/10.1016/j.matchar.2024.113675
Received 30 October 2023; Received in revised form 11 January 2024; Accepted 17 January 2024
Available online 18 January 2024

structure of metallic glasses allows atoms to move in response to stress, thus enhancing the flexibility of amorphous materials and their capacity for plastic deformation without cracking or breaking. Furthermore, the rapid solidification required for producing these materials prevents the formation of intermetallic compounds that contribute to brittleness in the material.

Cu—Ti alloys are strong candidates to use as filler materials to join the divertor components by brazing technique [7,8]. These alloys ensure efficient heat transmission and provide the necessary strength for the joint. However, the conventional fabrication process results in filler ribbons with limited flexibility, and these ribbons often fracture when adapted to the component's shape. The development of Cu—Ti metallic glasses in ribbon shapes could offer a solution to this issue, as it would impart the unique properties of these materials to the ribbons and allow for the scalability of the fabrication process using the melt-spinning technique.

Melt-spinning is a widely adopted technique for producing amorphous fibers and ribbons. In melt-spinning of amorphous metals, the molten metal is rapidly solidified through high-speed cooling to prevent crystallization and promote the formation of a non-crystalline structure. This technique presents several advantages over traditional methods of manufacturing amorphous metals, including higher cooling rates ($>10^6$ K/s), improved glass-forming ability, and the capability to produce continuous ribbons. Therefore, it holds promise as a technique for fabricating filler alloys with unique properties.

The fabrication of Cu based metallic glasses is currently under development. M. Ma et al. [9] study the effects on the microstructure, mechanical properties, and thermal stability of the $Zr_{34}Ti_{32}Cu_9Fe_4Be_{21}$ amorphous alloy gear castings adding different contents of remelting materials. The results indicated that the fracture strength of the amorphous alloy gear castings increases with the increasing remelting material content, whereas the plastic deformation ability decreases. S. Pang et al. [10] developed a novel $Ti_{50}Zr_{30}Co_{11}Cu_6M_3$ (M = Sn, V, Al) amorphous/nanocrystalline alloys with low liquidus temperatures developed as brazing filler alloys. The filler alloy enhanced the mechanical properties of titanium alloy brazed joints. D. Zhu et al. [11] produced an amorphous filler metal $Cu_{40}Ti_{40}Zr_{13}Ni_7$ using the melt-spinning technique for brazing high Nb–TiAl alloys and GH4169 superalloys. Their study revealed that the diffusion of elements between the substrates and the filler alloy intensified with increasing brazing temperature. At 960 °C, the joint exhibited a maximum shear strength of approximately 241.9 MPa. However, at higher brazing temperatures, the excessive presence of the $AlCu_2$(Ti, Zr) phase and the coarse Ti_2(Ni, Cu) phase negatively impacted the joint properties due to their inherent brittleness.

Previous work using Cu—Ti ribbons fabricated by melt-spinning studied the effects of different fabrication parameters on the ribbon flexibility and morphology and its influence on the microstructure and the mechanical properties of W-CuCrZr brazed joint [12]. The results indicated that Cu—Ti fillers with a length of <20 mm and a width of <2 mm can be fabricated. However, these dimensions are insufficient to cover the entire surface of the pipe. Additionally, crystallization of the ribbons was not completely inhibited, leading to the formation of Cu_3Ti matrix and Cu_4Ti precipitates. As a result, this phenomenon limited the flexibility and continuous formation of the ribbon.

This initial comprehensive study on wettability, interfacial microstructures, and the joining mechanism of tungsten-heavy alloy brazed joints can provide a deeper understanding of the joining process. Furthermore, it can serve as a guide for joining sintered dual/multi-phase refractory composites.

This article aims to analyze the amorphization effect of small additions of Zr, Ni, and V in the fabrication of Cu—Ti alloy ribbons, with the goal of enhancing their suitability for use in divertor joints. Additionally, the study explores the influence of various melt-spinning fabrication parameters, such as nozzle size and shape, ejection pressure, wheel speed, and the distance between the nozzle and the copper wheel, on the ultimate performance of melt-spun Cu—Ti ribbons. Subsequently, an in-depth investigation was conducted into the crystallinity, morphology, flexibility, microstructure and thermal properties of the melt-spun ribbons. Their potential impact on the brazeability of W-CuCrZr, for potential application in the future DEMO reactor, was also evaluated.

2. Experimental details

2.1. Materials and fabrication of flexible filler ribbons

Copper and titanium metallic powders were supplied by *Cymit Quimica,* copper powders, −325 mesh, +325 mesh, > 99% purity, and titanium powders, −200 mesh, 99.5%. Zirconium and nickel powder were supplied by *Alfa Aesar*, zirconium powder, −325 mesh, > 99% purity, and nickel powder −100 mesh, +99% purity. Vanadium powder was supplied by *Sigma Aldrich,* 325 mesh, and 99.5% trace metals basis. The metallic powder mixture underwent compaction by subjecting it to 750 (MPa) of pressure for a duration of 2 min, resulting in the formation of master alloy pellets with a diameter of 13 mm. This compaction process was executed using a hydraulic press, specifically the *Unicraft WPP 50 E*. Subsequently, the pellets were melted within a high vacuum furnace at 1100 °C for one hour to ensure homogenization.

The master alloy utilized in the production of fillers through the melt-spinning technique was derived from a bulk alloy synthesized in a high vacuum furnace, incorporating pure constituents to achieve the desired composition. The compositions explored in this study are detailed in Table 1. These alloys were chosen by keeping the balance of $Cu_{75}Ti_{25}$ at. % in which different proportions of amorphization materials (Zr, Ni, and V) were added to modify the solidification process mechanism and study its influence in the microstructure, crystallization, and mechanical properties.

The impact of fabrication parameters in the melt-spinning process on the properties of the fillers mentioned earlier was also investigated. To control the fabrication process, modifications were made to nozzle size and shape, ejection pressure, and wheel speed, as outlined in Table 2 [13]. This led to the analysis of seven distinct conditions across the three compositions. Two nozzle shapes were utilized: one rectangular and the other circular. The distance between the nozzle and the copper wheel remained consistent for all samples at 1.3 mm. The nominal cooling rate of the alloy is determined by the amount of material ejected and the wheel speed, both of which are subject to regulation by various parameters. Consequently, these factors play a critical role in the dimensions and microstructure of the ribbons, ultimately defining the physical and mechanical properties of the melt-spun ribbons.

Melt-spun ribbons were deeply characterized and finally used for brazing tungsten to CuCrZr alloy. Tungsten base material was provided by *Plansee,* in the form of a hot rolled recrystallized microstructure plate with a final thickness of 5 mm and purity of 99.99%. The CuCrZr alloy was supplied by *KME* also in plate form with the following composition Cu-balance (0.4–1.2) Cr (0.03–0.3) Zr wt% in accordance with EN (European Norms) and UNS (Unified Numbering System) standards.

2.2. Brazing process

A high vacuum furnace *(Navertherm)* was used for the brazing tests at the residual pressure of 10^{-6} mbar. Copper alloy and tungsten blocks of $6 \times 6 \times 5$ mm^3 were used as base materials. Before the brazing tests,

Table 1
Chemical composition of the base alloys. Samples with different amorphizing elements are named as A (Zr), B (ZrNi) and C (ZrNiV).

	Cu (at. %)	Ti (at. %)	Zr (at. %)	Ni (at. %)	V (at. %)
CuTiZr (A)	64	21	15	–	–
CuTiZrNi (B)	60	20	12	8	–
CuTiZrNiV (C)	63	21	5	5	5

Table 2
Conditions tested of melt-spinning technique. D is the internal diameter of the nozzle; v is the linear speed of the copper wheel and L is the width of the hole when it was used rectangular nozzles.

Condition (at. % - Cu balance)		D (mm)	v (m/s)	L (mm)
A	Cu21Ti15Zr	0.6–0.7	30	4
B1	Cu20Ti12Zr8Ni	0.7–0.8	30	6
B2	Cu20Ti12Zr8Ni	0.5	30	8.8
B3	Cu20Ti12Zr8Ni	0.7	35	–
C1	Cu21Ti5Zr5Ni5V	0.6–0.7	30	5
C2	Cu21Ti5Zr5Ni5V	0.5	35	8.8
C3	Cu21Ti5Zr5Ni5V	0.7	35	–

both base material exposed surfaces were polished with 4000-grid silicon carbide paper. Based on the thermal characterization of the studied alloys brazing cycles of 960 °C for 10 min were applied in all cases, and heating and cooling rates were set at 5 °C/min.

2.3. Characterization techniques

Flexibility and adaptability tests were conducted to assess these properties in the melt-spun ribbons. In this procedure, ribbons were positioned to cover the surface of the divertor or the first wall, simulating a pipe with a 20 mm diameter. This evaluation focused on assessing both the flexibility of the ribbons and their susceptibility to fracture.

The melt-spun ribbons underwent thermal characterization to determine their solidus, liquidus and crystallization temperatures. The first two parameters were determined through Differential Thermal Analysis (DTA) measurements using a *Setaram Thermal Analyser Setsys 16/18* instrument in an argon (Ar) atmosphere. The final parameter analyzes the temperature at which the transition from the amorphous structure to a crystalline arrangement commences. To achieve this, Differential Scanning Calorimetry (DSC) tests were conducted utilizing a *DSC 25* device from *TA Instruments* (New Castle, DE, USA). The tests were carried out in a temperature range from 0 to 700 °C with a constant heating rate of 10 °C/min. Each specimen underwent two consecutive scans to identify any irreversible effects within the sample, such as the crystallization process.

X-ray diffraction (XRD) tests were conducted utilizing a Cu Kα X-ray source in a *PANalytical X'Pert Pro MRD* diffractometer to assess the crystallinity of the ribbons and identify any potential crystalline phases present in the melt-spun ribbons. Furthermore, transmission electron microscopy (*HRTEM JEOL F200*) technique was also used to determine the presence of isolated crystalline phases and to resolve the microstructure in different zones of the ribbons. A focused ion beam (*Leica RES102*) equipment was used to prepare lamellas taken from the ribbons for TEM measurements.

Microstructural analysis of ribbons and brazed joints were carried out in the cross-section cut by Scanning Electron Microscopy (*SEM, S3400 Hitachi*) equipped with Energy Dispersive X-ray analysis (EDX). The cross-sections were metallographically prepared using the standard polishing technique [14].

3. Results

3.1. Characterization of Cu-Ti melt-spun ribbons

Fig. 1 illustrates the melt-spun ribbons obtained from the seven different conditions tested, each corresponding to one of the three compositions (A, B, and C). This study focused on examining the influence of various fabrication parameters. While compositions A and B displayed a degree of continuity in the melt-spun ribbons, composition C exhibited a flake-like particle morphology exclusively. The average dimensions of these melt-spun ribbons can be found in Table 3. It can be observed that the alloy CuTiZr yields ribbons of considerably greater

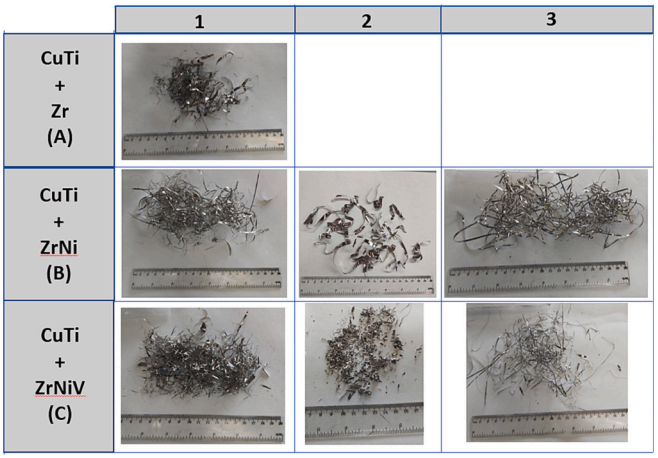

Fig. 1. Ribbons obtained after the melt-spinning process.

Table 3
Ribbons' dimensions of each condition.

Condition	Width (mm)	Length (mm)	Thickness (μm)
A	3.0 ± 0.5	> 800	37
B1	2.4 ± 1.2	> 160	87
B2	7.8 ± 0.8	> 160	50
B3	1.9 ± 0,1	> 2000	28
C1	2.2 ± 1.4	< 70	50
C2	1.0 ± 0.3	< 10	34
C3	0.6 ± 0.2	> 600	11

length, approximately 800 mm, but with a narrower width of 3 mm. Conversely, when the CuTiZrNi alloy composition was employed as the master alloy, it became possible to produce continuous ribbons, with lengths reaching up to a maximum of 2000 mm. In this case, the utilization of condition B3 allowed for the fabrication of continuous ribbons. It appears that the increase in wheel speed, from 30 m/s (conditions B1 and B2) to 35 m/s (B3), modified the ribbon solidification mechanism, enabling the production of longer ribbons. However, as a trade-off, these ribbons were narrower and thinner, measuring approximately 2 mm in width and 28 μm in thickness, in contrast to the 8 mm width and 50 μm thickness achieved when a lower wheel speed was employed. These dimensions differ from those reported in prior studies where CuTi melt-spun alloy produced ribbons measuring 50 mm in length and 1.8 mm in width [12]. It is clear that the addition of Zr and Ni elements results in alterations to the solidification mechanism, enabling the production of larger dimension ribbons that are better suited for the intended application.

The incorporation of vanadium to create the CuTiZrNiV alloy led to the formation of non-continuous ribbons, and, in some instances, only flake-like structures were produced (C2 condition). Furthermore, an increase in wheel speed had a positive effect on ribbon length, resulting in dimensions of 70 mm and 600 mm for conditions C1 and C3, respectively. However, in the case of C3, the ribbons became excessively narrow, measuring only 0.6 mm in width. Notably, only the C3 condition (0.7 mm thickness, 35 m/s wheel speed) produced ribbons of sufficient length for testing.

It appears that the introduction of vanadium (V) significantly increases the brittleness of the alloy, making it challenging to attain the desired level of flexibility. This effect was already shown by M. N. Srinivasan et al. [15] and A. Bell et al. [16]. They noted that the inclusion of vanadium introduced a degree of brittleness, preventing the attainment of superplasticity and complicating the melt-spinning process. Nevertheless, V as an alloying element can also yield advantages, as demonstrated by Y. Zhang et al. [17] and H. Ding et al. [18], who illustrated how the presence of V enhanced ductility at 1023 K and altered the

fracture mode from interlamellar to translamellar in the samples during the rapid cooling process of its fabrication.

With the exception of condition C, the dimensions of the fillers obtained closely resemble those found in commercial fillers designed for brazing applications. However, in the cases involving vanadium, the ribbons exhibit a more flake-like geometry, and in some instances, they do not exceed 10 mm in length or 1 mm in width. This limitation hinders their applicability as filler materials since they fail to adequately cover the surface requiring joining.

It should be noted, as depicted in Table 2, that longer samples are obtained in the cases involving circular nozzles (B3 and C3). On the other hand, when using a rectangular nozzle, wider ribbons are produced. Additionally, the wheel speed is a critical parameter that impacts not only the dimensions of the resulting ribbons but also their physical properties, as it will be discussed later on. In general, it is evident that as the wheel speed increases, the sample thickness decreases. This phenomenon has also been observed by other researchers [19,20]. This can be explained by the fact that at higher speeds, the same volume is projected onto a larger surface area of the wheel, leading to a reduction in thickness.

As outlined in the introduction section, the potential application for joining W-CuCrZr materials in the W monoblock to the divertor cooling pipe of the future DEMO fusion reactor necessitates the production of ribbons with specific mechanical properties, particularly adequate flexibility and adaptability to the joint shape. To assess their feasibility, an adaptability test was conducted using a 20 mm radius cylinder to simulate the cooling pipe. The results, presented in Table 4 and Fig. 2, indicated that most of the conditions exhibit sufficient length to cover the pipe surface, and almost all exhibit adequate flexibility to conform to the circular shape (Fig. 2). Only conditions C1 and C2 did not pass the adaptability test (Fig. 2b), highlighting a strong correlation between the production of ribbons with smaller dimensions and the lack of ribbon flexibility.

The crystallographic analysis of the melt-spun ribbons was conducted using X-ray diffraction patterns, as illustrated in Fig. 3. For samples A and B3, the XRD patterns reveal a predominant broad halo without discernible crystalline peaks, indicative of an amorphous structure within the ribbons. In sample A, a residual diffraction peak corresponding to a minor CuTi crystalline phase emerges within the 40–50° angle range. Nevertheless, a comparative examination of the CuTi reference material diffraction patterns with those of the investigated ribbons underscores a significantly lower crystallinity in our samples, characterized by the absence of numerous diffraction peaks. Moreover, the observed peaks exhibit low intensity, suggesting the presence of isolated crystalline domains or phases dispersed within the amorphous matrix.

In the case of sample C1, where V is present, a distinctively more crystalline structure is evident. This is marked by a series of diffraction peaks associated with CuTi and NiTi0.8Zr0.2 crystalline phases, along with Cu and Ni diffraction peaks.

The attainment of an amorphous matrix can be attributed to the inclusion of amorphizing elements in the alloy composition. These alloying elements can hinder the crystallization process during solidification due to their size differences, aided by the high cooling rates employed (approximately 10^6 K/s) [12].

Due to the amorphous structure, the formation of thermodynamically stable intermetallic compounds is inhibited, resulting in several beneficial effects on the properties of the melt-spun ribbons: 1) The solidification process on the copper wheel becomes more continuous, achieving lengths of over 2000 mm in some cases. This advancement holds the potential for upscaling the process. 2) Hardness and brittleness are reduced, rendering the melt-spun ribbons more flexible, enabling them to conform to curved surfaces. 3) A more uniform composition distribution is achieved, which, in principle, narrows the alloy melting range. This promotes a homogenous fusion during the brazing process, enhancing the wettability properties of the filler alloy, a crucial parameter in the brazing technique.

In terms of its applicability, a crucial requirement for the filler material is to possess a specific melting range and sufficient weldability to facilitate joint production. This necessity arises because the filler melting range should not exceed the CuCrZr melting point, which stands at 1085 °C [21]. Nonetheless, an excessively low melting range could lead to unintended melting of the joint during operational use. Therefore, an ideal filler should exhibit a broader temperature range (800–1000 °C), allowing for subsequent thermal treatments (such as solution annealing and aging) to restore the alloy microstructure and properties. This particular characteristic of the ribbons is indispensable for their practical application and functionality.

Thermal characterization of the melt-spun ribbons involved determining the melting range through DTA experiments. This data indirectly establishes the brazing window temperatures (solidus and liquidus temperatures, as summarized in Table 5) and crystallization temperature (T_x), which is obtained from DSC experiments. The crystalline temperature signifies the point at which the crystallization process commences within the amorphous matrix, subsequently leading to the loss of the distinctive properties that define the amorphous structure (as detailed in Table 6).

As for the melting range, all conditions, except for condition A, exhibit very similar values. The solidus temperatures range from 910 °C to 924 °C, and the liquidus temperatures range from 935 °C to 947 °C, resulting in an average melting range (the difference between solidus and liquidus temperatures) of approximately 25 °C. This narrow range is attributed to the uniform composition that characterizes the amorphous structure, eliminating the presence of distinct compositional phases requiring a diffusion phenomenon during heating to reach equilibrium melting composition. In the case of condition B2, an example of the obtained thermogram is illustrated in Fig. 4.

At this stage, only samples that exhibit sufficient flexibility, length, and adaptability to curved surfaces, such as conditions A, B1, B2, and B3, were selected for further characterization.

For the DSC tests, two distinct scans were conducted, covering a temperature range from 10 °C to 725 °C, aimed at analyzing the crystallization phenomenon (refer to Fig. 5). The initial scan reveals that, as the temperature exceeds the previously mentioned T_x, the crystallization process initiates, manifesting as an exothermic event (indicated by the blue line in Fig. 5 a-d). Subsequently, in the second scan, following completion of the initial one, no exothermic process is observed (as evident by the pink line in Fig. 5 a-d), and only the baseline is depicted, serving as clear evidence of the irreversible nature of the crystallization process.

Although all the samples undergo a multi-stage crystallization process, sample A exhibits crystallization initiation at 463 °C, whereas samples B1, B2, and B3 initiate crystallization at 410 °C, 430 °C, and 452 °C, respectively. In the case of sample A, once crystallization starts, the process appears to proceed more rapidly, as indicated by the exothermic process (black arrow). The use of a more complex alloy with a greater number of alloying elements appears to hinder the crystallization process. This explanation aligns with existing literature, as this process is governed by a solid-state diffusion mechanism, and the presence of a higher quantity of alloying elements hinders this

Table 4
Results of adaptability tests.

Cond	Adequate flexibility to fully cover the pipe surface	Enough length to cover the whole pipe
A	YES	YES
B1	YES	YES
B2	YES	YES
B3	YES	YES
C1	NO	NO
C2	NO	NO
C3	YES	YES

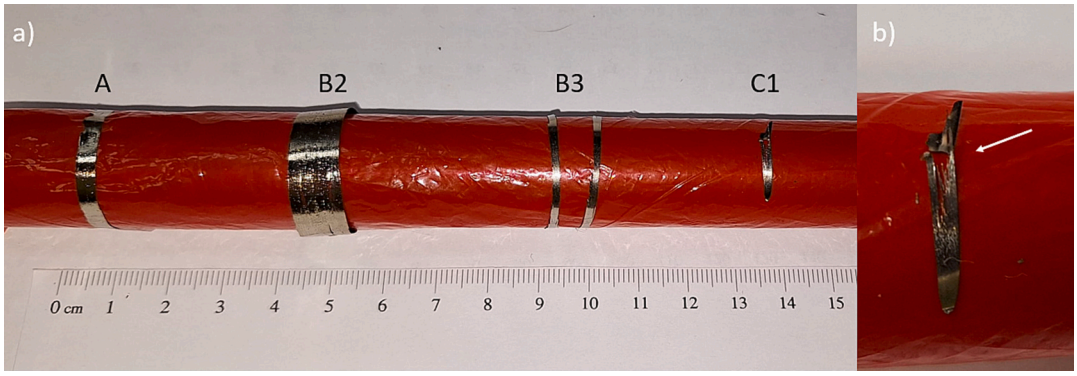

Fig. 2. a) Adaptability tests of A, B2, B3 and C1. b) Detail of the crack in sample C1. The pipe has a 20 mm radio.

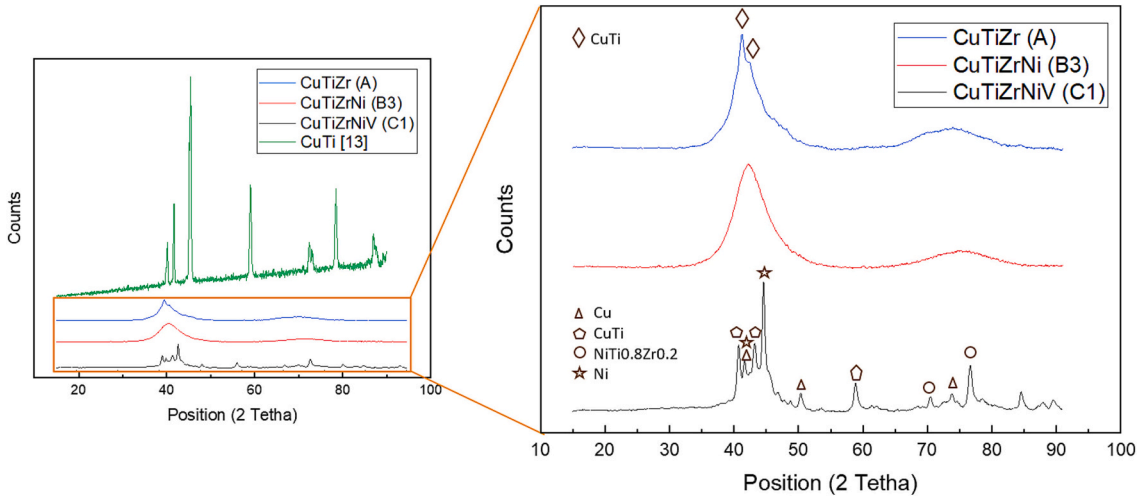

Fig. 3. XRD patterns of samples A, B3, C1 conditions and reference material [12].

Table 5
Solidus and liquidus temperatures for the fillers produced under conditions tested.

Condition	T_s (°C)	T_L (°C)
A	855	892
B1	910	935
B2	920	947
B3	924	940
C1	904	932
C2	914	941
C3	920	938

Table 6
Crystallization temperature of the different conditions tested.

Condition	T_x (°C)
A	463
B1	410
B2	430
B3	452

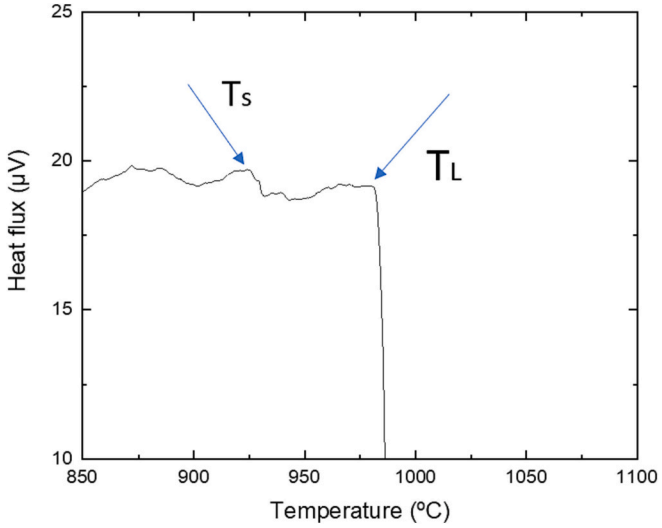

Fig. 4. Example of thermogram in the melting range region obtained by DTA technique of condition B2 ribbons in the heating ramp.

phenomenon. S. Zhang et al. [22] demonstrated a similar effect in their study on the impact of partial solubility of Cr and Ni in multi-component amorphous alloy ribbons. They observed that increasing the concentration of Cr is advantageous for amorphous state stabilization and reduces the probability of secondary crystallization.

It would be expected that conducting a heat treatment below T_x could lead to an enhancement in the flexibility and ductility of the samples by relieving the residual stresses generated during the ribbon manufacturing process.

The microstructures of the ribbons were also examined to determine

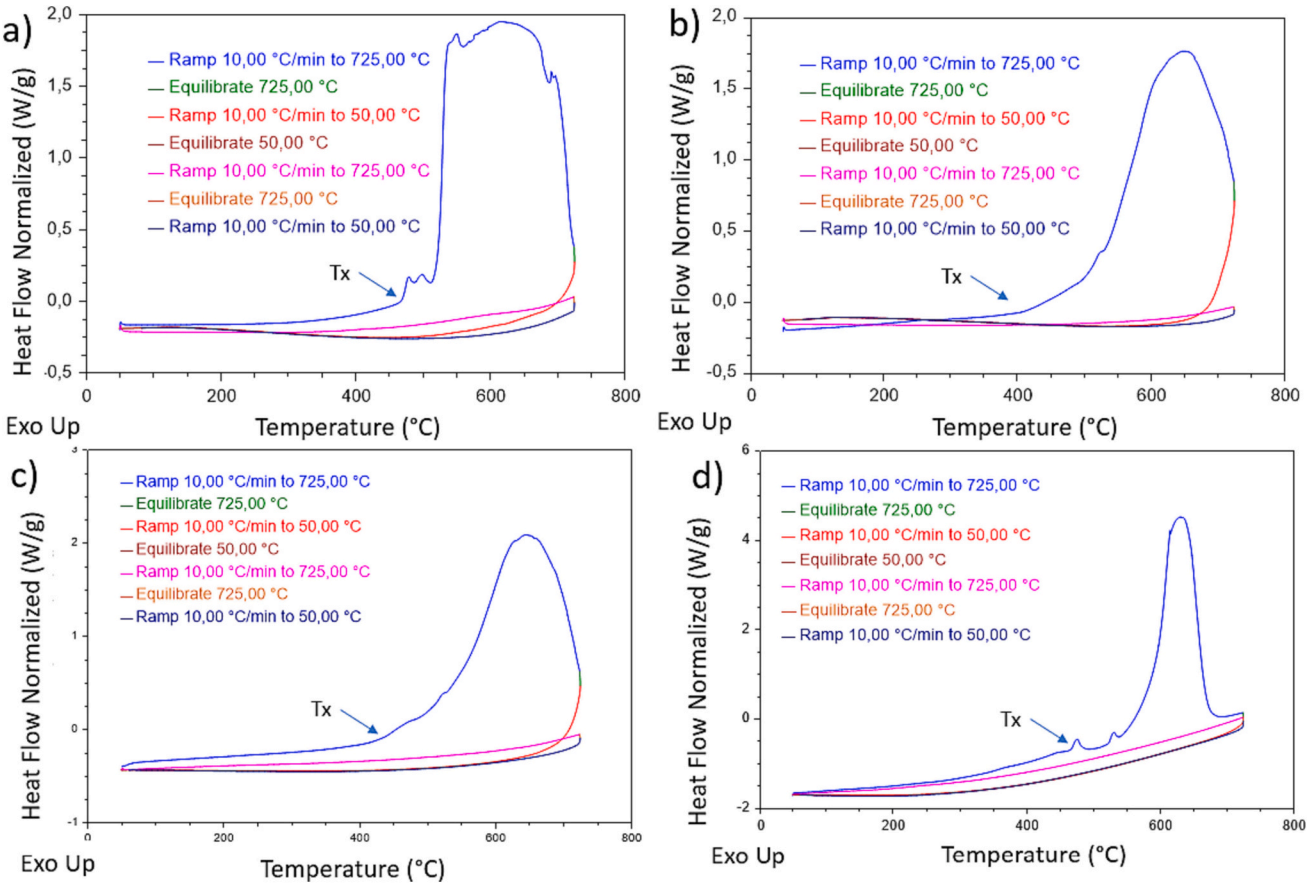

Fig. 5. DSC results of a) condition A, b) condition B1, c) condition B2 and d) condition B3.

the element distribution within the samples (see Fig. 6). SEM measurements using the electron backscatter detector revealed that, in most conditions, there was a uniform distribution of Cu, Ti, Ni, and Zr throughout the matrix, with no observable segregation. The elemental distribution observed in the EDS maps was in line with an amorphous filler distribution.

These results suggest that solidification occurred at a sufficiently high cooling rate to prevent the element redistribution typically associated with equilibrium solidification processes. Consequently, the formation of crystalline phases was not observed, except for the presence of small and isolated Zr-rich aggregates in all conditions.

To investigate deeper into the amorphous/crystalline nature of the matrix and the isolated precipitates, ribbons were subjected to TEM analysis. Fig. 7a, b, c, and d depict HRTEM micrographs along with the corresponding Selected Area Electron Diffraction (SAED) patterns for samples A, B1, B2, and B3, respectively. All samples exhibit a matrix

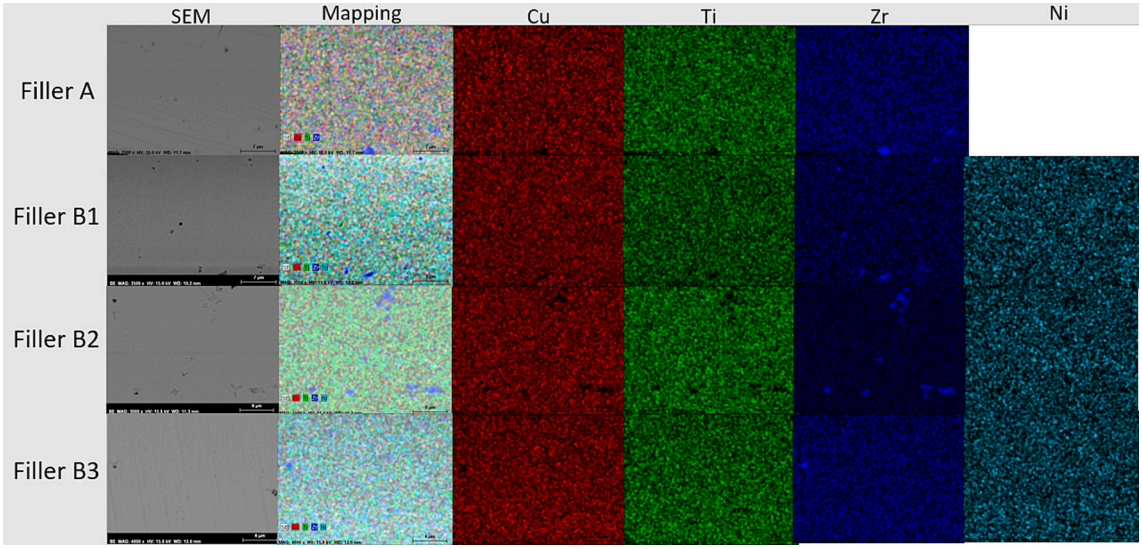

Fig. 6. SEM image and Elemental distribution of brazing fillers.

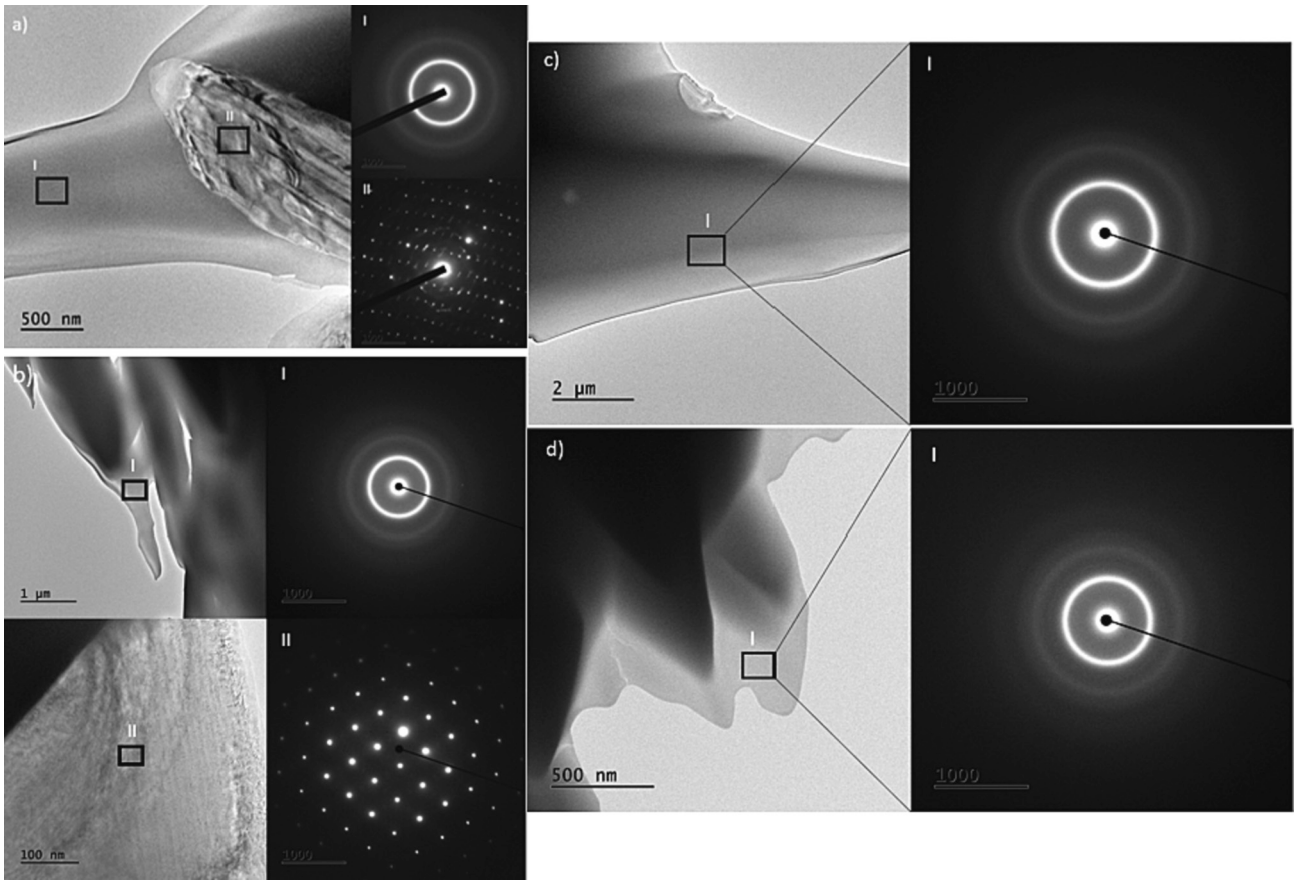

Fig. 7. HRTEM images of condition A. The inset in the right corner shows the corresponding SAED patterns. a) Cond A, b) cond B1, c) cond B2 and d) cond B3.

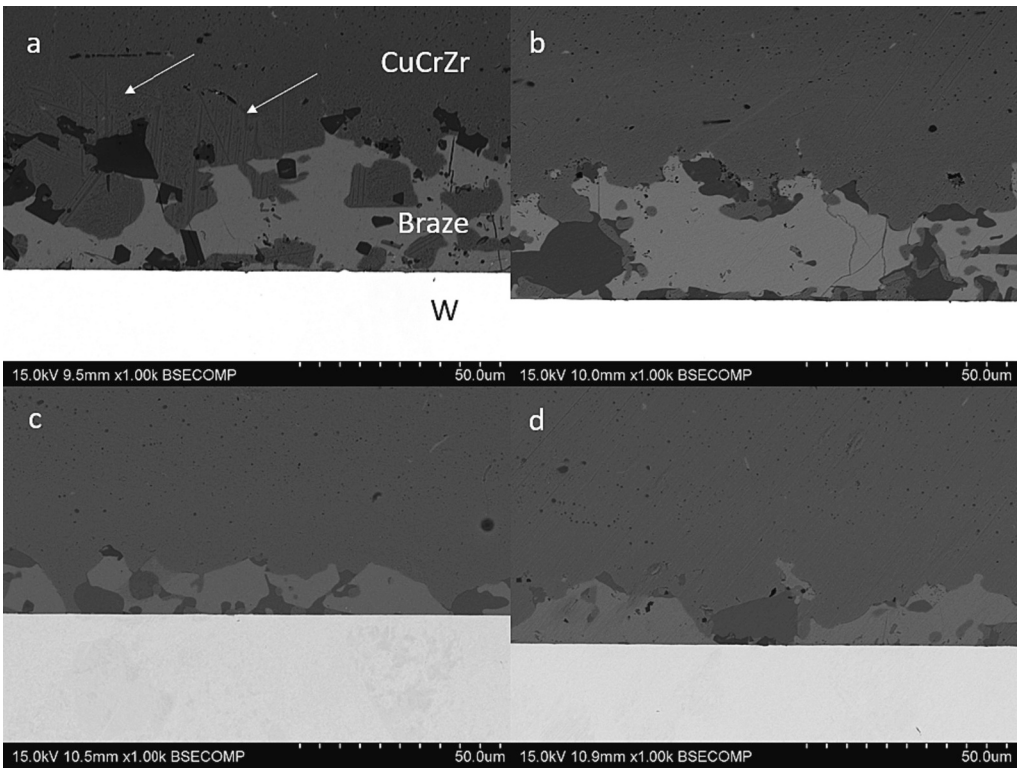

Fig. 8. Microstructures of brazed joints of using fillers fabricated under conditions a) A, b) B1, c) B2 and d) B3.

region, delineated within square I, while some samples (A and B1) reveal the presence of a small precipitate within square II. In the case of region, I, all figures display an absence of distinct features in the bright-field (BF) image and a diffused ring in the SAED pattern, thus confirming the amorphous nature of the as-spun ribbon matrix. This grainy and disordered appearance is a characteristic feature of such a structure [23,24].

However, the SAED analysis of precipitates diffraction pattern in region II indicates a crystalline phase compatible with $Cu_{51}Zr_{14}$ and $NiTi_{0.8}Zr_{0.2}$, for A and B1 samples, respectively.

3.2. Microstructural characterization of the brazed joints

Fig. 8 displays micrographs depicting the braze zone of W-CuCrZr joints employing ribbons fabricated through melt-spinning under conditions A, B1, B2, and B3 as filler materials. In all instances, there is full metallic continuity at both interfaces between the filler and the base materials. The brazing temperatures were maintained 40 °C above the liquidus temperature of each alloy, which facilitated proper wettability of the filler on W and CuCrZr, ensuring complete filling of the joint clearance.

The incorporation of various alloying elements in the alloy leads to the development of complex microstructures once equilibrium is achieved during the solidification and cooling stages of joint formation. These complex microstructures are particularly evident in conditions A and B1, where multiple precipitates and phases become visible (as seen in Fig. 8 a and b). In these cases, the alloys possess the lowest liquidus temperatures, which can result in limited interaction with the base materials, retaining the bulk of the alloying within the brazed region.

Condition A exhibits the presence of acicular structures (indicated by the white arrow in Fig. 8a), a feature not observed in the other conditions. These structures are associated with the formation of the Cu_4Ti phase within the Cu matrix, a phenomenon previously documented by other researchers when joining Cu alloys using crystalline Cu-Ti alloys [25].

It should also be noted that at this interface, the braze exhibits no physical or chemical interaction with W, resulting in a distinct and well-defined interface. This behavior is attributed to the inert nature of W at

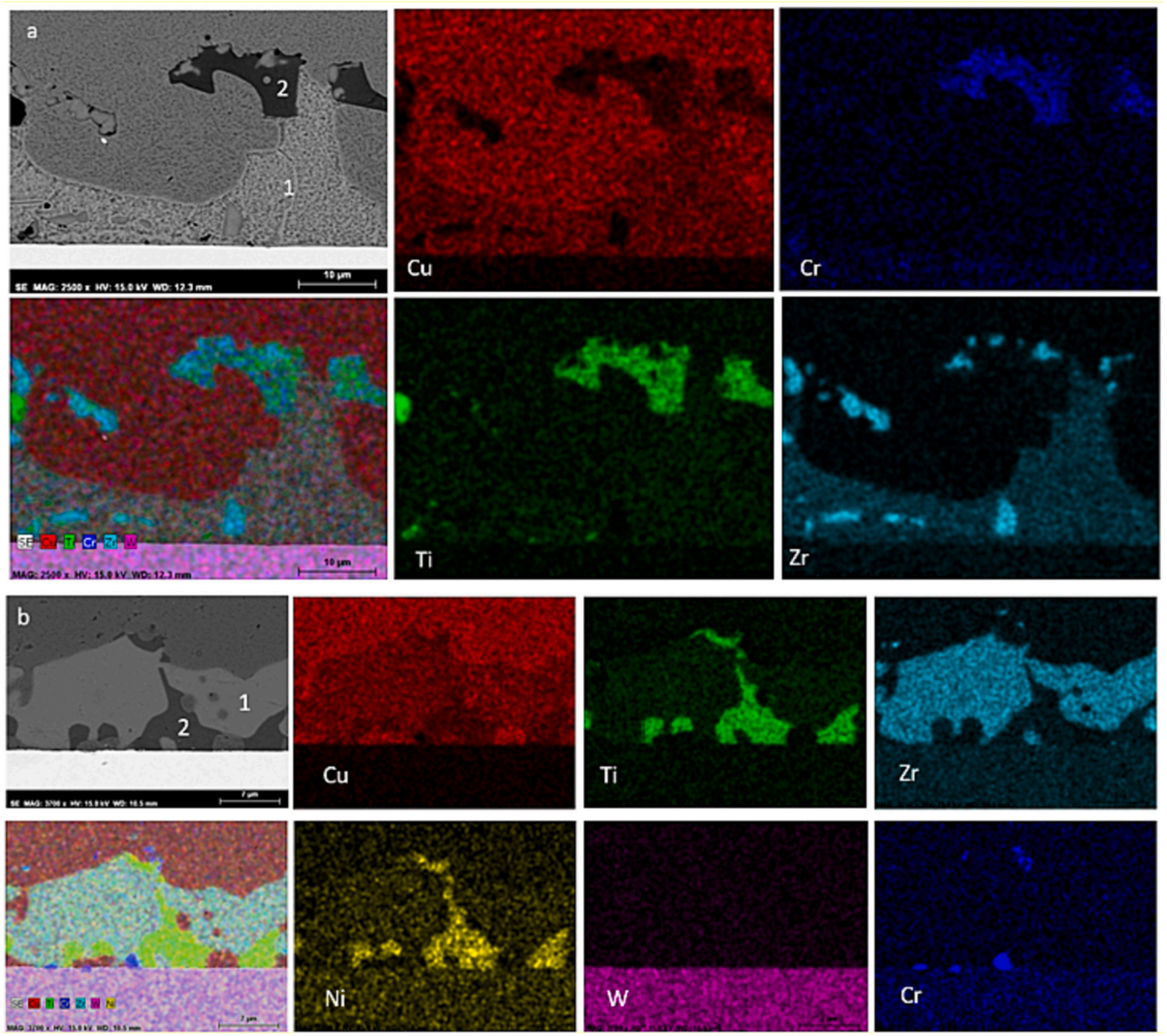

Fig. 9. Elemental mapping distribution of the braze for conditions of filler a) A and b) B2.

the elevated temperatures within a vacuum atmosphere.

Fig. 9 presents the elemental mapping distribution for conditions A and B1, exemplifying one microstructure type developed during the brazing process for each condition of filler. These mappings, in conjunction with point-specific EDS semi-quantitative analyses, offer detailed insights into the phase constituents and interfacial structures.

As illustrated in Fig. 9, both conditions exhibit similar structural features. The braze zone primarily consists of a copper-rich phase (labeled as number 1 in Fig. 9 a and b). Semi-quantitative EDX micro-analysis indicates a composition of 75Cu14Zr10Ti at.% for condition A and 72Cu18Zr5Ti4Ni at.% for condition B2. Additionally, in both samples, another phase with a darker appearance appears as isolated regions (labeled as number 2 in Fig. 9 a and b). This phase is rich in copper and titanium, with compositions of 41Cu51Ti5Cr3Zr at.% for condition A and 44Cu30Ti22Ni3Zr at.% for condition B2.

Condition B, which has Ni as alloying element, shows the presence of a third phase in the braze (labeled as number 3 in Fig. 10). According to the semiquantitative analysis, it has a 12Cu50Ti20Ni10Zr7Cr at.% composition.

4. Conclusion

The inclusion of Zr, Ni, and V alloying elements in a Cu—Ti alloy alters the solidification mechanisms during ribbon fabrication using the melt-spinning technique. The rapid cooling process and the presence of alloying elements of varying sizes hinder the crystallization process.

Consequently, the resulting ribbons exhibit an amorphous matrix with the presence of isolated crystalline precipitates, as confirmed by DRX and TEM analyses. These melt-spun ribbons exhibit excellent continuity, high flexibility and adaptability, particularly in simulating the pipe of a future reactor. The most favorable outcomes are achieved with a Cu20Ti12Zr8Ni at.% alloy composition and a wheel speed of 30 m/s, utilizing a rectangular nozzle measuring $0.5 \times 8.8\ mm^2$. Employing these processing parameters and alloy composition, ribbons measuring 70 mm in width and 160 mm in length are obtained.

Conversely, the inclusion of V in the alloy results in embrittlement, preventing the samples from attaining the desired dimensions or exhibiting sufficient flexibility.

SEM characterization reveals a homogeneous distribution of elements in the ribbons, which is consistent with an amorphous structure. Only small and isolated Zr crystalline precipitates are observed. This uniformity serves to narrow the melting range, enhancing the wettability of the braze and, therefore, is advantageous for its application in the brazing technique.

Joints fabricated using the best ribbons exhibit excellent metallic continuity, free from brazing defects. The microstructure predominantly comprises a copper-rich phase along with numerous precipitates of Cu-Ti-Ni-Zr composition.

CRediT authorship contribution statement

I. Izaguirre: Data curation, Formal analysis, Investigation, Methodology, Validation, Visualization, Writing – original draft. **J. de Prado:** Data curation, Formal analysis, Investigation, Methodology, Validation, Visualization, Writing – original draft. **J.J. Rosero-Romo:** Formal analysis, Investigation, Methodology, Validation, Visualization, Writing – original draft. **M. Sánchez:** Conceptualization, Formal analysis, Funding acquisition, Investigation, Project administration, Resources, Supervision, Writing – review & editing. **D. Salazar:** Formal analysis, Investigation, Methodology, Supervision, Validation, Visualization, Writing – original draft. **A. Ureña:** Conceptualization, Formal analysis, Funding acquisition, Investigation, Project administration, Resources, Supervision, Visualization, Writing – review & editing.

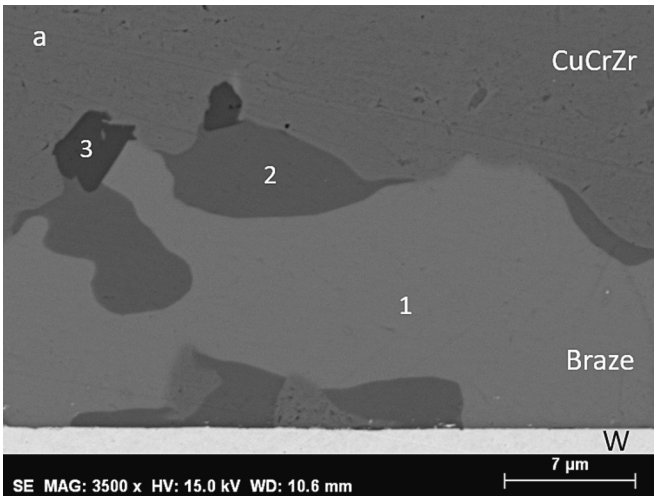

Fig. 10. Detail of the braze at the interface between W-CuCrZr of condition B2.

Declaration of competing interest

The authors declare the following financial interests/personal relationships which may be considered as potential competing interests: Ignacio Izaguirre reports financial support was provided by Rey Juan Carlos University.

Data availability

Data will be made available on request.

Acknowledgments

This work has been carried out within the framework of the EUROfusion Consortium, funded by the European Union via the Euratom Research and Training Programme (Grant Agreement No 101052200 — EUROfusion). Views and opinions expressed are however those of the author(s) only and do not necessarily reflect those of the European Union or the European Commission. Neither the European Union nor the European Commission can be held responsible for them. D. Salazar and J. J. Rosero-Romo acknowledge support from the EU Horizon 2020 research and innovation programme under Grant Agreement No. 862617 – Multi-Fun.

References

[1] R. Kembleton, M. Siccinio, F. Maviglia, F. Militello, Benefits and challenges of advanced divertor configurations in DEMO, Fusion Eng. Des. 179 (September 2021) (2022) 113120, https://doi.org/10.1016/j.fusengdes.2022.113120.
[2] D.N. Dongiovanni, T. Pinna, M.T. Porfiri, DEMO Divertor preliminary safety assessment, Fusion Eng. Des. vol. 169 (March) (2021) 112475, https://doi.org/10.1016/j.fusengdes.2021.112475.
[3] J.H. You, et al., Divertor of the European DEMO: engineering and technologies for power exhaust, Fusion Eng. Des. 175 (2022), https://doi.org/10.1016/j.fusengdes.2022.113010.
[4] G. Janeschitz, A. Antipenkov, G. Federici, Divertor Design and its Integration into the ITER Machine, This Conf.. [Online]. Available: http://scholar.google.com/scholar?hl=en&btnG=Search&q=intitle:Divertor+Design+and+its+Integration+into+the+ITER+Machine#0, 2000.
[5] J.H. You, M. Li, K. Zhang, Structural lifetime assessment for the DEMO divertor targets: design-by-analysis approach and outstanding issues, Fusion Eng. Des. vol. 164 (2021) 112203, https://doi.org/10.1016/j.fusengdes.2020.112203. November 2020.
[6] W. Wen, B.E. Ghidersa, W. Hering, J. Starflinger, R. Stieglitz, Heat pipe technology based divertor plasma facing component concept for European DEMO, Fusion Eng. Des. 164 (December) (2020) 2021, https://doi.org/10.1016/j.fusengdes.2020.112184.
[7] Z. Sun, L.X. Zhang, J.L. Qi, Z.H. Zhang, C.L. Tian, J.C. Feng, Brazing of SiO 2f /SiO 2 composite modified with few-layer graphene and invar using AgCuTi alloy, Mater. Des. 88 (2015) 51–57, https://doi.org/10.1016/j.matdes.2015.08.146.

[8] Q. Qiu, Y. Wang, Z. Yang, X. Hu, D. Wang, Microstructure and mechanical properties of TiAl alloy joints vacuum brazed with Ti-Zr-Ni-cu brazing powder without and with Mo additive, Mater. Des. 90 (2016) 650–659, https://doi.org/10.1016/j.matdes.2015.11.008.
[9] Z. Cai, et al., Effect of adding remelting materials on the properties of die-cast Zr-based amorphous alloy gear castings, J. Non-Cryst. Solids 581 (December 2021) (2022) 121428, https://doi.org/10.1016/j.jnoncrysol.2022.121428.
[10] X. Bai, et al., Novel Ti–Zr–Co–Cu–M (M = Sn, V, Al) amorphous/nanocrystalline brazing fillers for joining Ti–6Al–4V alloy, Mater. Charact. 196 (October 2022) (2023) 112607, https://doi.org/10.1016/j.matchar.2022.112607.
[11] C. Yang Jiang, X. Qiang Li, B. Wan, D. Zhi Zhu, S. Guan Qu, C. Yang, Microstructure evolution and mechanical properties of TiAl/GH536 joints vacuum brazed with Ti–Zr–Cu–Ni filler metal, Intermetallics 142 (December 2021) (2022) 107468, https://doi.org/10.1016/j.intermet.2022.107468.
[12] I. Izaguirre, J. de Prado, M. Sánchez, D. Salazar, A. Ureña, Development of flexible filler ribbons by melt spinning for joining W to CuCrZr material for heat sink application, Fusion Eng. Des. 181 (January) (2022) 0–6, https://doi.org/10.1016/j.fusengdes.2022.113214.
[13] G. Geng, D. Wang, W. Zhang, L. Liu, A.M. Laptev, Fabrication of Cu–Ni–Si alloy by melt spinning and its mechanical and electrical properties, Mater. Sci. Eng. A 776 (November 2019) (2020) 138979, https://doi.org/10.1016/j.msea.2020.138979.
[14] American Society for Testing and Materials, Standard Guide for Preparation of Metallographic Specimens 1 vol. 03, no. July, 2001.
[15] M.N. Srinivasan, S.D. Little, Effect of melt spinning variables on the structure and properties of a dispersion strengthened Al-Fe-V-Si alloy, Scr. Metall. Mater. 32 (8) (1995) 1153–1158, https://doi.org/10.1016/0956-716X(95)00117-E.
[16] A. Bell, H.A. Davies, Solid solubility extension in Cu-V and Cu-Cr alloys produced by chill block melt-spinning, Mater. Sci. Eng. A 226–228 (1997) 1039–1041, https://doi.org/10.1016/s0921-5093(96)10854-6.
[17] K. Du, et al., Elimination of room-temperature brittleness of Fe–Ni–Co–Al–Nb–V alloys by modulating the distribution of Nb through the addition of V, Mater. Sci. Eng. A 855, no. July (2022) 143848, https://doi.org/10.1016/j.msea.2022.143848.
[18] X. Xu, et al., Effect of V on the microstructure and brittle-to-ductile transition of directionally solidified high-Nb TiAl alloy, Intermetallics 142 (August 2021) (2022) 107455, https://doi.org/10.1016/j.intermet.2021.107455.
[19] Y.W. Kim, T.H. Nam, The effect of the melt spinning processing parameters on the martensitic transformation in Ti50-Ni35-Cu15 shape memory alloys, Scr. Mater. 51 (7) (2004) 653–657, https://doi.org/10.1016/j.scriptamat.2004.06.023.
[20] S. Öztürk, S.E. Sünbül, K. Icin, Effects of melt spinning process parameters and wheel surface quality on production of 6060 aluminum alloy powders and ribbons, Trans. Nonferrous Met. Soc. China (English Ed.) 30 (5) (2020) 1169–1182, https://doi.org/10.1016/S1003-6326(20)65287-6.
[21] C. Li, et al., Characterization on the melting failure of CuCrZr cooling tube of W/cu monoblocks during plasma operations in EAST, Nucl. Mater. Energy 25 (2020) 100847, https://doi.org/10.1016/j.nme.2020.100847.
[22] S. Zhang, Z. Zhang, P. He, Y. Gao, X. Liang, Microstructure and properties of melt-spun AlYNiCr multi-component amorphous alloy ribbons through partial substitution of Cr for Ni, Mater. Lett. 317 (February) (2022) 132089, https://doi.org/10.1016/j.matlet.2022.132089.
[23] Y. Zhang, H. Wang, T. Zhai, T. Yang, Y. Qi, D. Zhao, Hydrogen storage characteristics of the nanocrystalline and amorphous Mg-Nd-Ni-Cu-based alloys prepared by melt spinning, Int. J. Hydrog. Energy 39 (8) (2014) 3790–3798, https://doi.org/10.1016/j.ijhydene.2013.12.139.
[24] S. Zhang, Z. Zhang, C. Chen, X. Li, Y. Gao, X. Liang, Relation between quenching wheel speed and microstructure, thermal stability and corrosion resistance of quinary Al-Ni-Y-Co-Si high entropy metallic glass ribbons prepared by melt spinning, J. Non-Cryst. Solids 601 (November) (2022) 2023, https://doi.org/10.1016/j.jnoncrysol.2022.122049.
[25] J. de Prado, M. Sánchez, A. Ureña, Wettability study of a Cu-Ti alloy on tungsten and EUROFER substrates for brazing components of DEMO fusion reactor, Mater. Des. 99 (2016) 93–101, https://doi.org/10.1016/j.matdes.2016.03.054.